Adaptive beamforming combined with decision theory-based detection for ultrasound localization microscopy

Alexandre Corazza, Pauline Muleki-Seya, Arthur Chavignon, Olivier Couture, Adrian Basarab, Barbara Nicolas

Adaptive beamforming combined with decision theory-based detection for ultrasound localization microscopy

Alexandre Corazza
CREATIS UMR 5220, U1206
Univ Lyon, INSA-Lyon,
Université Claude Bernard Lyon 1,
UJM-Saint Etienne, CNRS, Inserm
F-69100, Villeurbanne, France
Alexandre.Corazza@creatis.insa-lyon.fr

Pauline Muleki-Seya
CREATIS UMR 5220, U1206
Univ Lyon, INSA-Lyon,
Université Claude Bernard Lyon 1,
UJM-Saint Etienne, CNRS, Inserm
F-69100, Villeurbanne, France
Pauline.Muleki-Seya@creatis.insa-lyon.fr

Arthur Chavignon
Laboratoire d'Imagerie Biomédicale
Sorbonne Université, CNRS, INSERM
Paris, France
Arthur.Chavignon@sorbonne-universite.fr

Olivier Couture
Laboratoire d'Imagerie Biomédicale
Sorbonne Université, CNRS, INSERM
Paris, France
Olivier.Couture@sorbonne-universite.fr

Adrian Basarab
CREATIS UMR 5220, U1206
Univ Lyon, INSA-Lyon,
Université Claude Bernard Lyon 1,
UJM-Saint Etienne, CNRS, Inserm
F-69100, Villeurbanne, France
Adrian.Basarab@creatis.insa-lyon.fr

Barbara Nicolas
CREATIS UMR 5220, U1206
Univ Lyon, INSA-Lyon,
Université Claude Bernard Lyon 1,
UJM-Saint Etienne, CNRS, Inserm
F-69100, Villeurbanne, France
Barbara.Nicolas@creatis.insa-lyon.fr

***Abstract*—Ultrasound Localisation Microscopy (ULM) is an imaging framework which consists in tracking microbubbles (MBs) on ultrasound (US) images to estimate their trajectory and thus the map of the vascular network. ULM algorithms takes as input US images usually beamformed with the delay-and-sum (DAS) method. In a previous study, we have shown that adaptive beamforming enhances the results of ULM on simulated data by detecting more MBs and localizing them more precisely. In another study, we introduced a new MB detection method based on decision theory. In this paper, adaptive beamformers such as Capon, pDAS and iMAP combined to this detection method are applied on *in vivo* rat brain data. Results show that this combination allow to identify more MBs and thus to represent more vessels in the ULM vascular network map.**

***Index Terms*—Ultrasound Super-Resolution, adaptive beamforming, microbubble identification, decision theory**

I. Introduction

ULM is a super-resolution imaging method providing information on vascular network structures and flow velocity by detecting, localising and tracking microbubbles (MBs). Its interest has been validated on rat [1] and human [2] brain as part of the study of stroke and brain diseases. It has also been applied to detect tumors [3] [4] and to monitor anticancer therapy [5] [6]. An example of ULM framework is described on Fig. 1. First, a liquid solution containing MBs is injected by vein (Fig. 1a). While the MBs are moving in the vascular network, carried away by the blood flow, US signals are acquired over time (Fig. 1b). These signals are beamformed to obtain US images (Fig. 1c). The tissue is filtered (Fig. 1d), generally with a singular value decomposition (SVD) [7], in order to facilitate the MBs identification (Fig. 1e). The centroid of the identified MBs are localized with a precision beyond the diffraction limit (Fig. 1f). Finally, the centroid coordinates at different times are paired to track each MB (Fig. 1g) to build the vascular network map by accumulating the MBs trajectories (Fig. 1h).

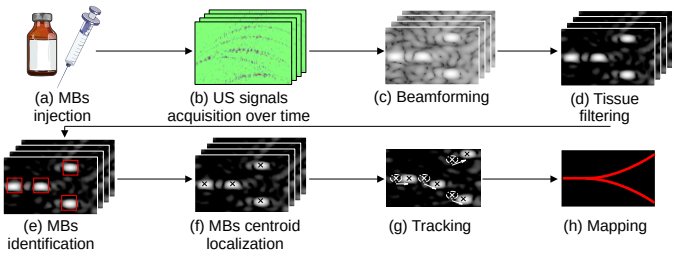

Fig. 1: ULM framework example.

A prerequisite for ULM is to acquire ultrasound (US) images during a sufficient time such that the MBs can move through a maximum of vessels. Thus, there is a trade-off between acquisition time and the completion of the vascular network map. To deal with this trade-off, adaptive beamforming can be a solution. Indeed, the properties of US images could have a significant influence on ULM outputs. For instance, the minimum variance beamformer provides a better resolved point spead function (PSF) [8]. Other beamforming methods such as pDAS [9] or iMAP [10] highlight the MBs and attenuate the speckle and noise components on the US images. We studied the effect of these beamformers in [11] and showed

that adaptive beamformers enhance the localisation precision and the detection rate on a simulated dataset. However, the benefits on *in vivo* studies were less evident. In addition to this study, we also introduced a new MB identification method based on decision theory [12]. In this paper, we are pursuing our work by combining adaptive beamforming with this MB identification method and evaluate the results on an experimental rat brain dataset.

II. Material and method

A. In vivo dataset

The *in vivo* dataset is provided by the Performance Assessment of Localization Algorithms (PALA) toolbox [13], is available at https://zenodo.org/record/7883227. The RF data are acquired with a linear US probe emitting at 15 MHz (L22-14v, Verasonics, USA) and an US research scanner (Vantage 256, Verasonics, USA) on a rat brain during MB injections of 50 μL every 30 seconds. The acquisition process lasted 3 minutes and 20 seconds with a frame rate of 1000 Hz, with 3 plane waves tilted at -7°, 0° and 7° angles.

B. Beamforming methods

Each scatterer that backscatters an echo from the plane wave excitation provides information about its echogenicity through the energy along the echo wave front. The first step of beamforming is to isolate this wave front by rephasing the received signals. The principle is based on time-arrival delay of an echo coming from coordinates (x, z) on each piezoelectric sensor along the linear probe. The second step is to sum the rephased signals, eventually weighted by a vector $\mathbf{w}$ manually set, to extract the pixel intensity at the coordinates (x, z). This method is called Delay-And-Sum (DAS) [14]. The difference with adaptive beamforming is the weighting vector $\mathbf{w}$ that is adaptive, *i.e.* computed from the rephased signals in different ways depending on the beamforming method:

- the minimum variance, also known as Capon, is based on the rephased signal variance minimization to attenuate eventual disturbing sources [15] [8]. In practice, this strategy provides a thinner PSF,
- the pDAS method [9] computes the weighting vector through an auto-correlation approximation of the rephased signal. In practice, this calculation rule leads to an attenuation of uncorrelated signal component such as noise and speckle. A parameter p defines the autocorrelation order. The method is referred to as 2pDAS for $p = 2$,
- the iMAP beamformer [10] models the rephased signal as the sum of a constant component corresponding to the backscattered amplitude and a random Gaussian noise. By applying a maximum *a posteriori* strategy, the mean and standard deviation of a Gaussian distribution that maximize the similarity with the distribution of the rephased vector are estimated to isolate the constant component. In practice, the noise and speckle are attenuated. To estimate the mean and variance, the algorithm iterates through a loop. The method is referred to as 2iMAP for 2 iterations.

C. Microbubble identification methods

In the literature, three MB identification methods can be encountered. The first, based on the intensity, consists in finding the local maximas higher than a threshold empirically chosen [16] [17]. An equivalent method is to set a number N of MBs to detect per image and to select only the N higher local maximas [1]. However, some MBs intensities are lower than noise. Thus, the second identification method is intensity-independant and is based on normalized cross-correlation (NCC) [18] [19]. The aim of this method is to detect structures similar in shape to a MB model, often estimated as a Gaussian shape [19], with simulation [18] or experimentally by imaging a wire cross-section [20] [21]. A threshold τ is applied on the NCC results to extract the structures with the highest similarities compared to the MB model. We proposed a third method based on decision theory (DT) with the Neyman-Pearson criterion [12], which is independant on intensity and PSF shape. Its principle is to study each pixel along the time dimension. The temporal signal for one pixel is modeled as the sum of a Gaussian noise induced by tissue movement and electronical noise and a constant component corresponding to a MB passage on the pixel. The decision theory tools allow to compute an adaptive threshold different for each pixel in order to isolate the constant component with a false alarm rate α_0 set by the user. It provided a more complete and better-resolved vessel map [12].

D. Ultrasound Localization Microscopy method and beamforming

The ULM framework used is available on the GitHub page of the PALA toolbox https://github.com/AChavignon/PALA related to the work in [13]. The NCC and decision theory based identification methods can be added to this toolbox with the code available on the GitHub page https://github.com/CorazzaAlexandre/Microbubble_detection. The beamforming methods are also available at https://github.com/CorazzaAlexandre/PALA_Beamforming. The ULM parameters used are summarized in the Table I. Note that the SVD filter is applied on the RF data, before beamforming since pDAS and iMAP can highlight tissue components and make it difficult to filter after beamforming. To limit the computation time of this step, we used the randomized SVD [22]. Note that intensity-based MB identification is not suitable due to MB slight attenuation with pDAS or iMAP. Either the NCC identification is not used due to its inability to link some vessels as highlighted in [12].

III. Results and discussion

The beamformers are applied to the *in vivo* rat brain RF signals after SVD filtering. An example for each beamforming method is given in Fig. 2. It can be seen by taking the DAS as reference that Capon reduces the PSF size, and that 2pDAS and 2iMAP attenuate the speckle. The effect on the decision theory identification is studied through the threshold maps on Fig. 3. As expected, for DAS, some low threshold areas

TABLE I: ULM parameters.

Parameter	Value
Tissue filtering	SVD (cutoff: 10)
Beamforming	DAS, Capon, pDAS or iMAP
US image pixel size	$\lambda = 100\mu$m
MB identification	Intensity (N=100 MBs per images) NCC (Gaussian PSF model, τ = 0.6) DT (α_0 = 0.1%)
ROI size	5λ
Isolation	3 local maximas per ROI maximum
Localisation	Radial symmetry based method [23]
Tracking	Hungarian algorithm max linking distance: 2λ, minimal track length: 10 images
Density map pixel size	$\lambda/10$

are drawn in the vessels where MBs are moving and high threshold in the tissue areas. With Capon, the threshold map is equivalent to DAS. However, with 2pDAS and particularly with 2iMAP, these low threshold areas are more resolved and a new one appears in the long vessels at the bottom of the image. There is a high MB concentration in these long vessels, and it has been discussed in [12] that this could be a limit for the decision theory method. Indeed, frequent passage of bubbles over a pixel biases the estimation of the noise mean and standard deviation respectively by the median and the median absolute deviation (MAD). Thus, it is interesting to see that adaptive beamforming is able to overcome this limit. An hypothesis is that 2pDAS and 2iMAP enhance the signal-to-noise ratio (SNR) which helps to distinguish noise from MBs, and thus to correctly estimate the noise mean and standard deviation. The vacular network map provided by the ULM algorithm with DT identification for each beamforming methods are presented on the Fig. 4(c) to (f). For visual comparison, the results with the intensity and NCC detections, both with DAS beamforming are shown on Fig. 4(a) and (b). The first map on Fig. 4(a) has a lack of detection and the second on Fig. 4(b) fails to connect some vessels between them (see areas Z_i). The maps obtained with the DT detection on Fig. 4(c) to (f) are quite similar, but some vessels indicated by the arrows are more filled with to 2pDAS and 2iMAP. To quantify these enhancement, different quantitative metrics are shown on Fig. 5. The saturation curves obtain with the different beamformers on Fig. 5a can be considered equivalent. The track length and velocity statistics on Fig. 5b and c indicate that the identified MBs lead to equivalent tracking qualities with each beamforming method. However, the resolution estimated by the Fourier Ring Correlation (FRC) [24] is slighly lower with the adaptive beamforming passing from 13 μm with DAS to 13.9 μm with Capon and 15.1 μm with 2pDAS and 2iMAP. Although FRC is robust to noise, this degradation in resolution can be caused by temporally correlated noise, *i.e.* undesirable temporally recurrent trajectories, *e.g.* the two artefacts at the top right and left corners. It is discussed in [24] that these artifacts can bias the FRC. To conclude, although the images show areas with enhanced visibility (white arrows), there is currently no overall quantitative criterion for quantifying this improvement.

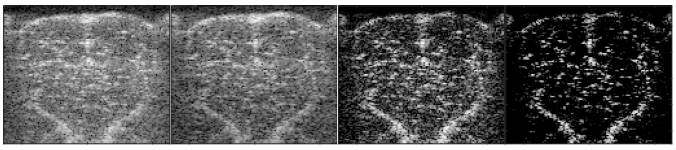

(a) DAS (b) Capon (c) 2pDAS (d) 2iMAP

Fig. 2: Rat brain US images with different beamformers (log scale, dynamic of 60dB).

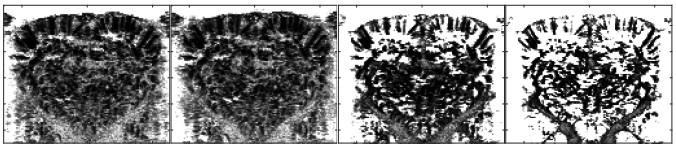

(a) DAS (b) Capon (c) 2pDAS (d) 2iMAP

Fig. 3: Threshold maps computed on 800 images (linear scale between 0 and 1).

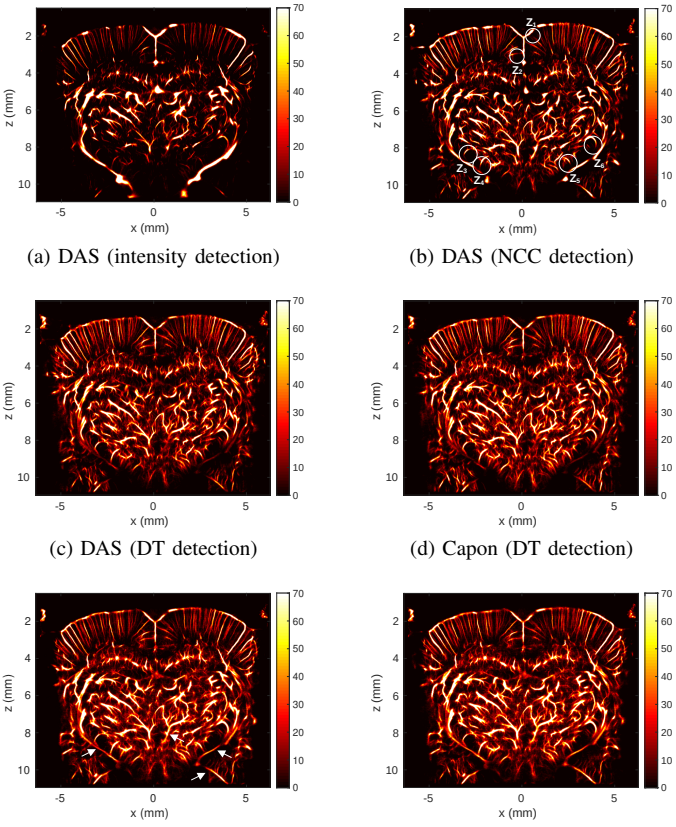

(a) DAS (intensity detection) (b) DAS (NCC detection)

(c) DAS (DT detection) (d) Capon (DT detection)

(e) 2pDAS (DT detection) (f) 2iMAP (DT detection)

Fig. 4: ULM results with different beamformers.

IV. Conclusion

In this study, adaptive beamforming was applied to image a rat brain in the context of ULM. Different beamformers were used, such as Capon which reduces the PSF size and 2pDAS or 2iMAP which attenuate the noise and speckle. The quantitative metrics show that the tracking qualities are equivalent with all beamforming methods. Visual analysis show that 2pDAS and

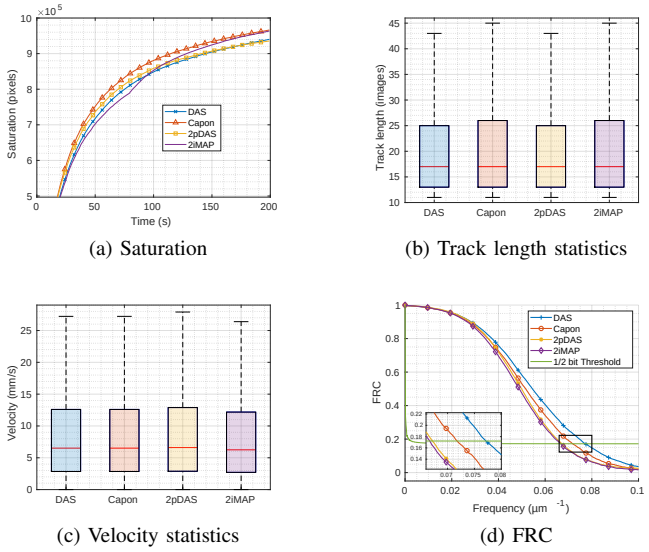

(a) Saturation (b) Track length statistics

(c) Velocity statistics (d) FRC

Fig. 5: Quantitative metrics of ULM results for different beamformers and different identification methods.

2iMAP allow to identify and track more MBs. In perspective, it would be interesting to apply these adaptive beamformers on additional *in vivo* datasets to generalize these conclusions.

ACKNOWLEDGMENTS

This work was supported by the LABEX CELYA (ANR-10-LABX-0060) and LABEX PRIMES (ANR-11-LABX-0063) of Université de Lyon, within the program "Investissements d'Avenir" (ANR-11-IDEX-0007) operated by the French National Research Agency (ANR). This work was partly funded by France Life Imaging (grant ANR-11-INBS-0006).

REFERENCES

[1] O. Couture, V. Hingot, B. Heiles, P. Muleki-Seya, and M. Tanter, "Ultrasound Localization Microscopy and Super-Resolution: A State of the Art," *IEEE Transactions on Ultrasonics, Ferroelectrics and Frequency Control*, vol. 65, no. 8, pp. 1304–1320, Aug. 2018. [Online]. Available: https://hal.archives-ouvertes.fr/hal-02344318

[2] C. Demené, J. Robin, A. Dizeux, B. Heiles, M. Pernot, M. Tanter, and F. Perren, "Transcranial ultrafast ultrasound localization microscopy of brain vasculature in patients," *Nature Biomedical Engineering*, vol. 5, no. 3, pp. 219–228, 2021. [Online]. Available: http://dx.doi.org/10.1038/s41551-021-00697-x

[3] F. Lin, J. D. Rojas, and P. A. Dayton, "Super resolution contrast ultrasound imaging: Analysis of imaging resolution and application to imaging tumor angiogenesis," in *2016 IEEE International Ultrasonics Symposium (IUS)*, 2016, pp. 1–4.

[4] F. Lin, S. Shelton, D. Espindola, J. Rojas, G. Pinton, and P. Dayton, "3-d ultrasound localization microscopy for identifying microvascular morphology features of tumor angiogenesis at a resolution beyond the diffraction limit of conventional ultrasound," *Theranostics*, vol. 7, pp. 196–204, 01 2017.

[5] T. Opacic, S. Dencks, B. Theek, M. Schulte, D. Ackermann, A. Rix, T. Lammers, E. Stickeler, S. Delorme, G. Schmitz, and F. Kiessling, "Motion model ultrasound localization microscopy for preclinical and clinical multiparametric tumor characterization," *Nature Communications*, vol. 9, 04 2018.

[6] D. Ghosh, F. Xiong, R. Mattrey, S. Sirsi, and K. Hoyt, "Monitoring early tumor response to vascular targeted therapy using super-resolution ultrasound imaging," in *2017 IEEE International Ultrasonics Symposium (IUS)*, 2017, pp. 1–1.

[7] C. Demené, T. Deffieux, M. Pernot, B. F. Osmanski, V. Biran, J. L. Gennisson, L. A. Sieu, A. Bergel, S. Franqui, J. M. Correas, I. Cohen, O. Baud, and M. Tanter, "Spatiotemporal Clutter Filtering of Ultrafast Ultrasound Data Highly Increases Doppler and fUltrasound Sensitivity," *IEEE Transactions on Medical Imaging*, vol. 34, no. 11, pp. 2271–2285, 2015.

[8] B. M. Asl and A. Mahloojifar, "Contrast enhancement and robustness improvement of adaptive ultrasound imaging using forward-backward minimum variance beamforming," *IEEE Transactions on Ultrasonics, Ferroelectrics, and Frequency Control*, vol. 58, no. 4, pp. 858–867, 2011.

[9] M. Polichetti, F. Varray, J.-C. Béra, C. Cachard, and B. Nicolas, "A nonlinear beamformer based on p-th root compression—application to plane wave ultrasound imaging," *Applied Sciences*, vol. 8, no. 4, 2018. [Online]. Available: https://www.mdpi.com/2076-3417/8/4/599

[10] T. Chernyakova, D. Cohen, M. Shoham, and Y. C. Eldar, "IMAP Beamforming for High-Quality High Frame Rate Imaging," *IEEE Transactions on Ultrasonics, Ferroelectrics, and Frequency Control*, vol. 66, no. 12, pp. 1830–1844, 2019.

[11] A. Corazza, P. Muleki-Seya, A. W. Aissani, O. Couture, A. Basarab, and B. Nicolas, "Microbubble detection with adaptive beamforming for ultrasound localization microscopy," in *2022 IEEE International Ultrasonics Symposium (IUS)*, 2022, pp. 1–4.

[12] A. Corazza, P. Muleki-Seya, A. Basarab, and B. Nicolas, "Microbubble identification based on decision theory for ultrasound localization microscopy," *IEEE Open Journal of Ultrasonics, Ferroelectrics, and Frequency Control*, vol. 3, pp. 41–55, 2023.

[13] B. Heiles, A. Chavignon, V. Hingot, P. Lopez, E. Teston, and O. Couture, "Performance benchmarking of microbubble-localization algorithms for ultrasound localization microscopy." *Nat Biomed Eng*, 2022. [Online]. Available: https://doi.org/10.1038/s41551-021-00824-8

[14] V. Perrot, M. Polichetti, F. Varray, and D. Garcia, "So you think you can das? a viewpoint on delay-and-sum beamforming," *Ultrasonics, Elsevier*, vol. 111, p. 106309, 2021. [Online]. Available: https://www.sciencedirect.com/science/article/pii/S0041624X20302444

[15] P. Stoica and R. Moses, *Spectral Analysis of Signals*, 2005.

[16] M. A. O'Reilly and K. Hynynen, "A super-resolution ultrasound method for brain vascular mapping," *Medical Physics*, vol. 40, no. 11, pp. 1–7, 2013.

[17] D. Ackermann and G. Schmitz, "Detection and tracking of multiple microbubbles in ultrasound B-mode images," *IEEE Transactions on Ultrasonics, Ferroelectrics, and Frequency Control*, vol. 63, no. 1, pp. 72–82, 2016.

[18] C. Bourquin, J. Porée, F. Lesage, and J. Provost, "In vivo pulsatility measurement of cerebral microcirculation in rodents using dynamic ultrasound localization microscopy," *IEEE Transactions on Medical Imaging*, vol. 41, no. 4, pp. 782–792, 2022.

[19] P. Song, J. D. Trzasko, A. Manduca, R. Huang, R. Kadirvel, D. F. Kallmes, and S. Chen, "Improved super-resolution ultrasound microvessel imaging with spatiotemporal nonlocal means filtering and bipartite graph-based microbubble tracking," *IEEE Transactions on Ultrasonics, Ferroelectrics, and Frequency Control*, vol. 65, no. 2, pp. 149–167, 2018.

[20] K. Christensen-Jeffries, R. J. Browning, M.-X. Tang, C. Dunsby, and R. J. Eckersley, "In vivo acoustic super-resolution and super-resolved velocity mapping using microbubbles," *IEEE Transactions on Medical Imaging*, vol. 34, no. 2, pp. 433–440, 2015.

[21] K. Christensen-Jeffries, S. Harput, J. Brown, P. N. Wells, P. Aljabar, C. Dunsby, M. X. Tang, and R. J. Eckersley, "Microbubble Axial Localization Errors in Ultrasound Super-Resolution Imaging," *IEEE Transactions on Ultrasonics, Ferroelectrics, and Frequency Control*, 2017.

[22] P. Song, J. D. Trzasko, A. Manduca, B. Qiang, R. Kadirvel, D. F. Kallmes, and S. Chen, "Accelerated Singular Value-Based Ultrasound Blood Flow Clutter Filtering with Randomized Singular Value Decomposition and Randomized Spatial Downsampling," *IEEE Transactions on Ultrasonics, Ferroelectrics, and Frequency Control*, vol. 64, no. 4, pp. 706–716, 2017.

[23] R. Parthasarathy, "Rapid, accurate particle tracking by calculation of radial symmetry centers," *Nature Methods*, vol. 9, no. 7, pp. 724–726, 2012.

[24] V. Hingot, A. Chavignon, B. Heiles, and O. Couture, "Measuring image resolution in Ultrasound Localization Microscopy," *IEEE Transactions on Medical Imaging*, 2021.